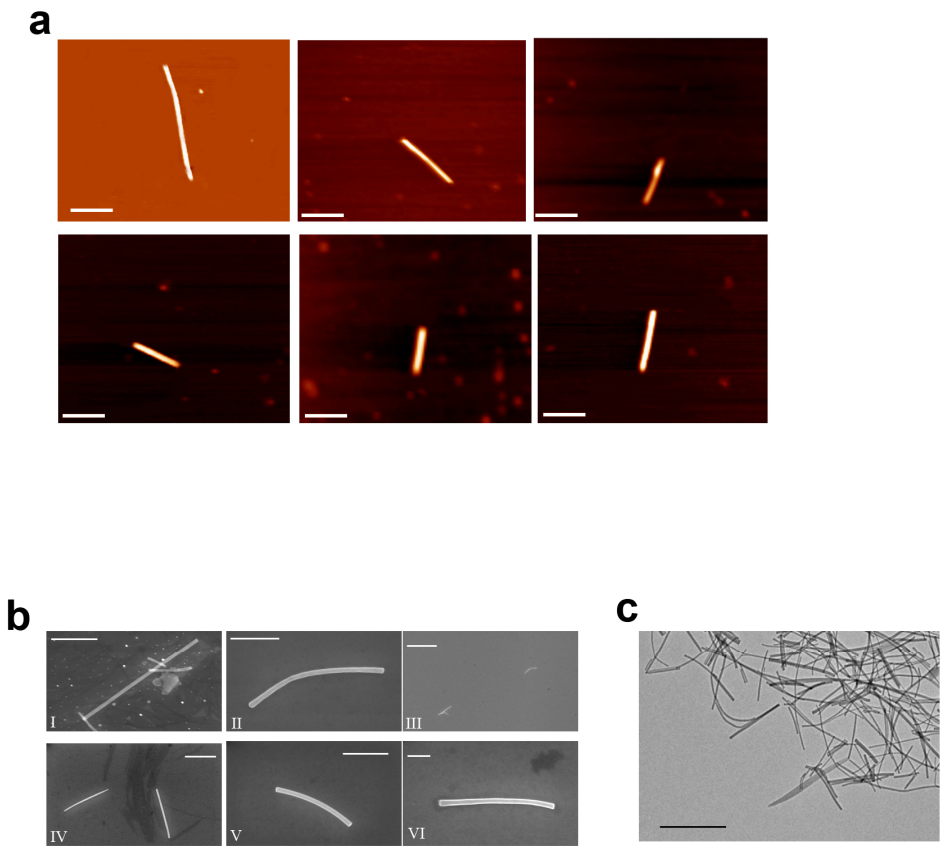

Supplementary Figure S1. (a) AFM images of single DNA nanotubes (scale bar - 1 μm). (b) SEM images of single DNA nanotubes (scale bar I - 700 nm, II - 500 nm, III – 5 μm, IV - 1μm, V – 500 nm, VI – 100 nm). (c) TEM image of a collection of single DNA nanotubes (scale bar – 2 μm).

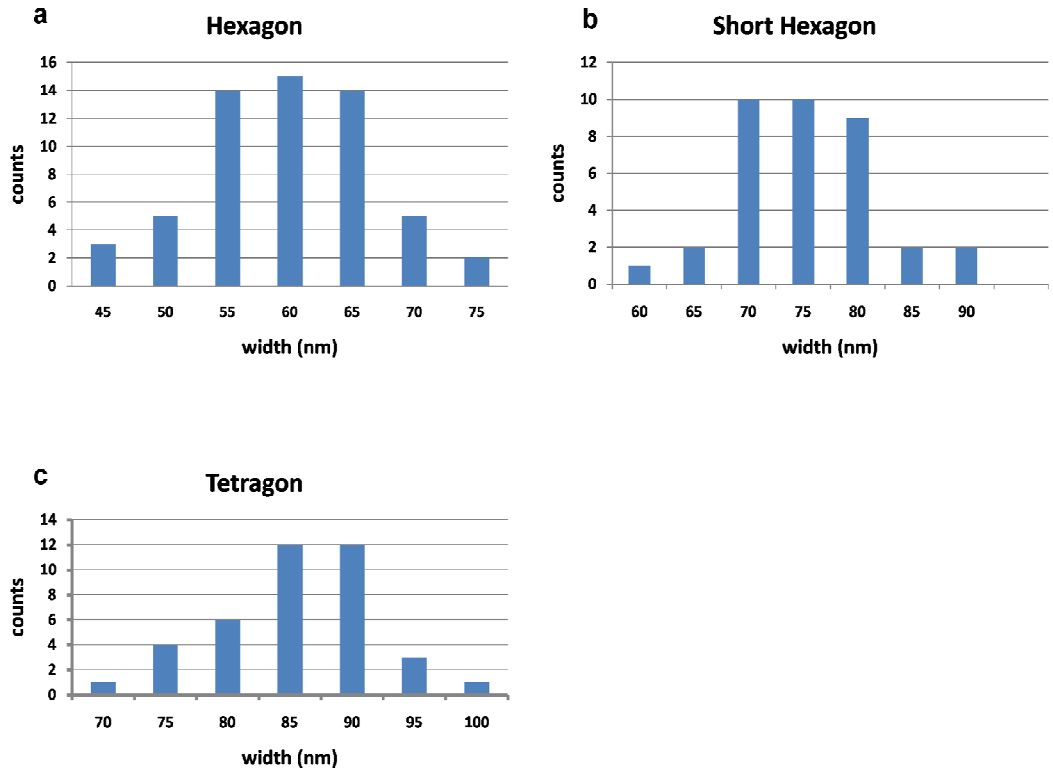

Supplementary Figure S2. Histograms showing the widths distribution of:

(a) The DNA nanotubes generated upon hybridization of the hexagon nucleic acid (**1**).

(b) The DNA nanotubes generated upon hybridization of the short hexagon nucleic acid (**4**).

(c) The DNA nanotubes generated upon hybridization of the tetragon nucleic acid (**5**).

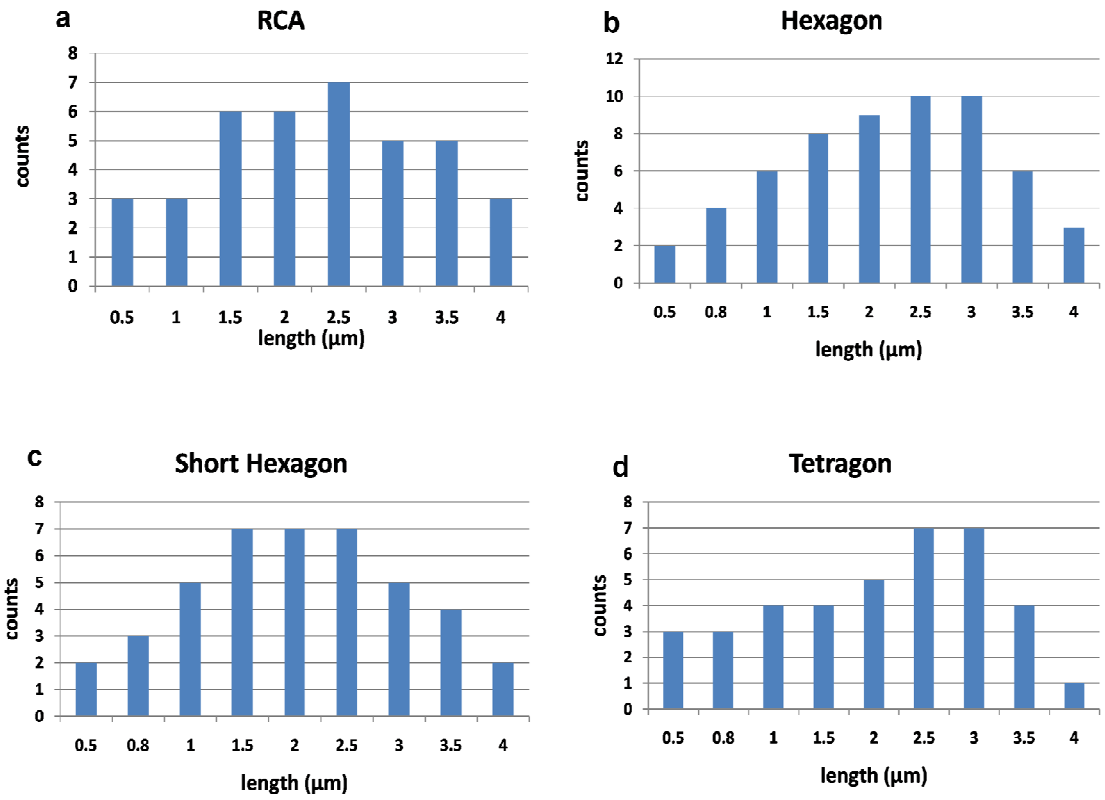

Supplementary Figure S3. Histograms showing the lengths distribution of:

(a) The RCA chains.

(b) The DNA nanotubes generated upon hybridization of the hexagon nucleic acid (**1**).

(c) The DNA nanotubes generated upon hybridization of the short hexagon nucleic acid (**4**).

(d) The DNA nanotubes generated upon hybridization of the tetragon nucleic acid (**5**).

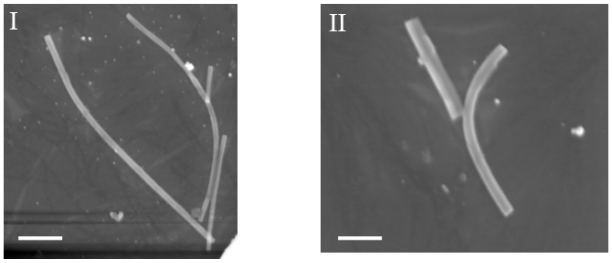

Supplementary Figure S4. HR-SEM images of single DNA nanotubes consisting of the small "hexagon" nucleic acid subunit, (**4**), generated in the presence of a partially complementary RCA tape (scale bar I – 300 nm, II- 100 nm).

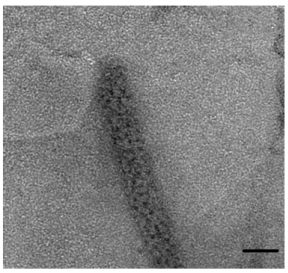

Supplementary Figure S5. HR-TEM image of a DNA nanotube consisting of the "tetragon" nucleic acid subunit, (**5**), decorated with Au NPs (1.4 nm) tethered to each of the tetragon subunits (scale bar – 50 nm).

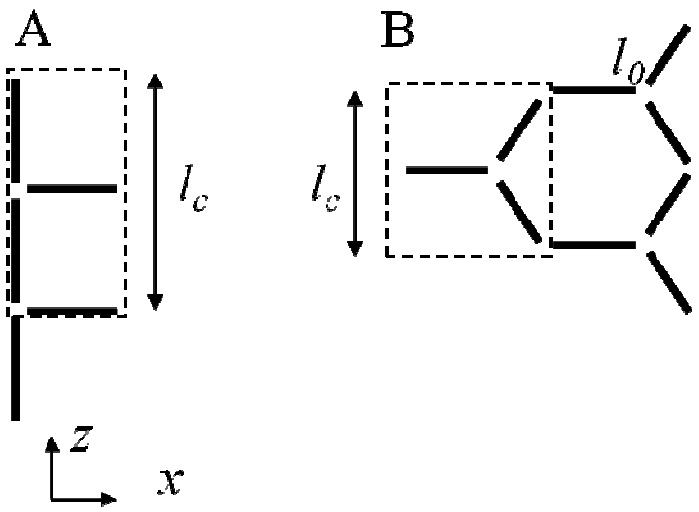

Supplementary Figure S6. Schematic of two dsDNA mesh geometries: (A) tetragonal (B) hexagonal.

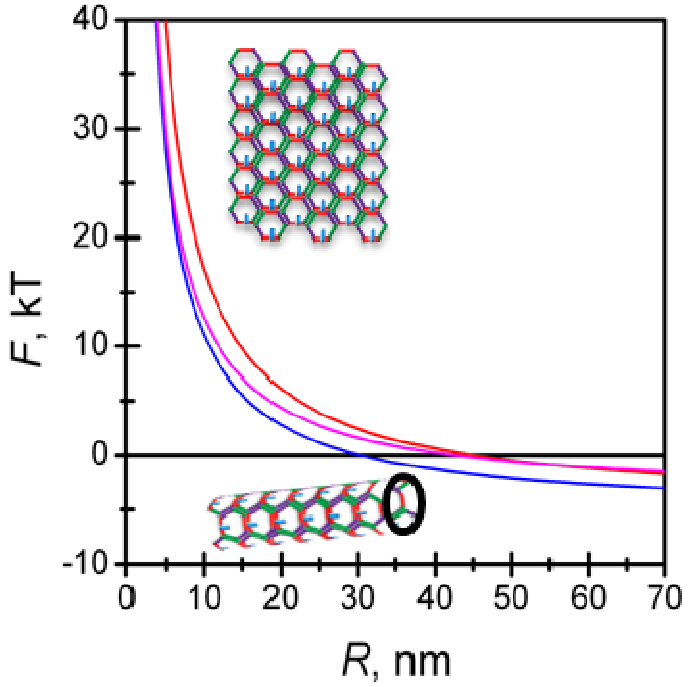

Supplementary Figure S7. Free energy for different tube radii shown per band of unit length along the tube. The points where the free energy turns from positive (low radii) to negative (high radii) marks the first radii where tube formation is thermodynamically favorable. Curves correspond to several mesh sizes and geometries: large hexagons (blue) small hexagons (magenta) and tetragons (red).

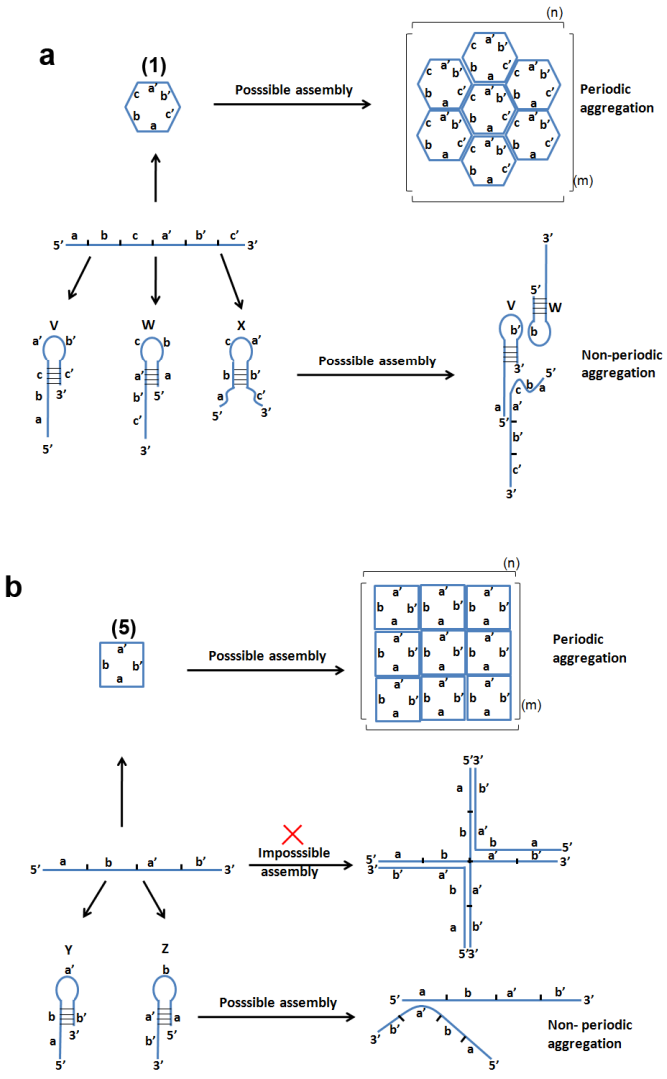

Supplementary Figure S8. Possible hybridization scheme for DNA strands used in this study, leading to hexagonal sheets with 3-way junctions (a) or square lattice with 4-way junctions (b) The scheme shows different hybridization possibilities, but only one scheme in each case can lead to the formation of extended sheets, thereby displacing all other constructs.

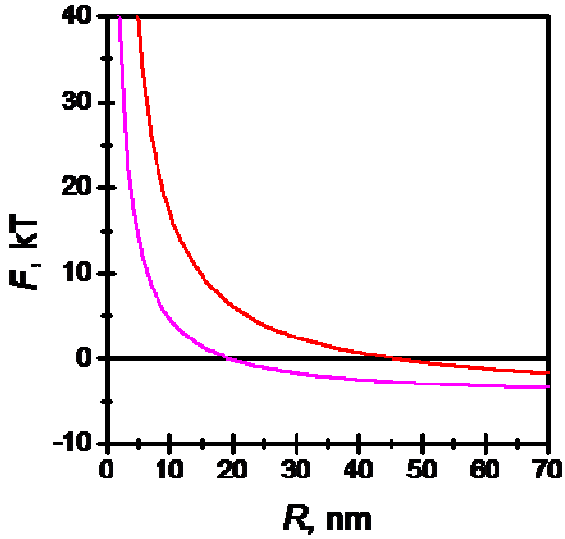

Supplementary Figure S9. Free energy for different tube radii shown per band of unit length along the tube. Compared here are different assumptions on the junction bending rigidity. The points where the free energy turns from positive (low radii) to negative (high radii) marks the first radii where tube formation is thermodynamically favorable. Curves correspond to: tetragons assuming $\kappa_J \approx \kappa_D$ (red) and tetragons assuming $\kappa_J < \kappa_D$ (magenta).

Supplementary methods

Estimates for the bending rigidity of DNA sheets

We start with estimating the bending modulus of meshes of hexagonal and tetragonal geometries. We make the simplifying assumption that elastic contributions from duplexed DNA segments are additive, and that their energy is harmonic with respect to (small) curvature deformations (as for an elastically deformed rod, or with analogy to Hooke's law for a spring). In this model, junctions (vertices) do not contribute to the bending energy; this assumption can be relaxed, as further detailed below. If junctions are highly flexible, or if the unstressed configuration of DNA tiles is not flat, additional contributions to the elastic energy must be considered[34].

Supplementary Figure S6 (a) shows the tetragonal mesh, with bending occurring along the *x* axis, and the tube forms along the *z* axis. It is convenient to consider a unit cell of one DNA strand length l_0 in the *x* direction and $2l_0 = l_c$ in the *z* direction; we note that only part of the two strands on the edge (5 out of 15 bp's) gain from hybridizing in tube closing (the other strand simply displaces another, the RCA). In this simple mesh, the energy of bending the unit cell into a tube of radius R is related to the energy of bending two dsDNA strands of length l_0 that lie in parallel to the *x* axis. We approximate dsDNA in the sheet as a worm-like chain, whose bending rigidity κ_D is related to the persistence length l_p of DNA in solution, $\kappa_D = kTl_p$, where kT is thermal energy. The elastic energy per unit (tetragonal) cell is, using eq. 1, the free energy associated with bending two dsDNA segments of length l_0, so that:

$$F_{el}^{tet,cell} = 2\times\frac{1}{2}kTl_p l_0 \frac{1}{R^2} \qquad \text{(S5)}$$

For a band of height l_c curved in a tube of radius R, the total bending energy is, therefore,

$$F_{el}^{tet} = 2\pi kTl_p \frac{1}{R} \qquad \text{(S6)}$$

The corresponding cohesion energy $F_b = -l_c\varepsilon$ is simply the hybridization free energy of the previously unhybridized parts of the tetragon. Supplementary Figure S6 (b) shows the unit cell of the hexagonal mesh. Here, a convenient unit cell is of height $l_c = \sqrt{3}l_0$ and a width along the *x* axis of $1.5l_0$, as shown by the dashed lines. Within this unit cell there is one segment bent along the cylindrical axis, and two others that are skewed at an angle. In fact, these two DNA segments are more moderately bent as they form part of a helical bend around the tube, with a radius of curvature 4 times larger than for the horizontally bent segment. The total accumulated bending energy within this unit cell is therefore:

$$F_{el}^{hex,cell} = \frac{1}{2}kTl_p l_0 \left[\frac{1}{R^2} + \frac{2}{(4R)^2}\right] \qquad \text{(S7)}$$

So that for the energy of a band of the tube with the same height the bending free energy is:

$$F_{el}^{hex} = \pi kTl_p \frac{3}{4}\frac{1}{R} \qquad \text{(S8)}$$

Here, again, the hybridization energy corresponds to one edge (only) of the hexagon. We note that smaller or larger hexagons will only differ in the corresponding cohesion energy per unit cell, while the elasticity per unit cell in the z direction remains the same. These calculations neglect the twist contribution to the elastic energy. The torsion modulus of

DNA has not been extensively studied as the persistence length[35], but in general this contribution to the total free energy of mesh bending is expected to be small, as long as the radius of curvature is not very small (*R* smaller than ca. 10nm).

Numerical estimates

To compare with experiments, we require values for the cohesion energy, as well as for the persistence length l_p. The persistence length of double stranded B-DNA has been extensively studied under solution conditions that are close to physiological. However, there is less information available on its value under low salt conditions, and experimental estimates vary quite substantially. We use here $l_p = 70nm$ for salts concentration of 10^{-3} M, based on a compilation of data[30-32].

Estimates for the binding free energy associated with the formation of dsDNA also vary quite widely at high salt concentration, and estimates are even less well determined for the low salt conditions used in our experiments. We used the compilation of data and subsequently derived unified parameters of SantaLucia[29] to obtain estimates of the duplexing free energy gain in the different mesh geometries and sizes, according to the base-pair sequence, and at a salt concentration of 10^{-3} M. We note, however, that our comparisons are quite sensitive to the parameters used, so that with the current knowledge of these parameters, any comparison should necessarily be regarded as only semi quantitative. Using these available data for DNA base-pairing and binding energies, it is possible to estimate the following free energies for different DNA sheets:

Large Hexagon:

$l_0 = 8.83nm$;

$\Delta G(15bps, 1M\ salt) = -14.54Kcal/mol$

$\Delta G(15bps, 10^{-3} M\ salt) = -2.73Kcal/mol = -4.45kT$

Small hexagon:

$l_0 = 5.88nm$;

$\Delta G(10bps, 1M\ salt\ ?) = -9.64Kcal/mol$

$\Delta G(10bps, 10^{-3} M\ salt) = -1.77Kcal/mol = -2.88kT$

Tetragon:

$l_0 = 5.1nm$;

$\Delta G(5bps, 1M\ salt) = -6.57Kcal/mol$

$\Delta G(5bps, 10^{-3} M\ salt) = -2.64Kcal/mol = -3.87kT$

Finally, strand displacement and liberation that occurs upon tube closure should be followed by a favorable entropic contribution, that we estimate at ca. -1kT per released side, added to the total cohesion free energy.

Using these estimates, it is now possible to plot the free energy per unit cell length along the DNA tube. At the point that the free energy turns from positive to negative, tube closure is thermodynamically favored. Figure S7 shows curves for the 3 mesh sizes and geometries examined in the model.

We find that the predicted tube radius increases in the order:

$R_{\text{large hexagons}} < R_{\text{small hexagons}} < R_{\text{tetragons}}$. With no adjustable parameters, the number as which it becomes probable to find tube closure are also very close to the experimentally found tube sizes: $R^*_{\text{large hexagons}} = 30nm$, $R^*_{\text{small hexagons}} = 42nm$ and $R^*_{\text{tetragons}} = 46nm$. As already discussed, these numbers are sensitively dependent on the numerical values of the bending and cohesion energies involved in tube formations.

DNA strand association, junctions, and sheet topology

The formation of the DNA nanotubes by the folding of two-dimensional sheets, generated by the single-stranded DNAs is based on the hexagon-type or tetragon-type complementarities of the strands. In view of the complementarities features of the single strands, one could, however, envisage alternative oligomerization schemes as outlined in Supplementary Figure S8. For example, besides the hexagon-type array of (**1**), the intermolecular hybridization of (**1**) could yield hairpin structures (V, W, X) that could hybridize through "kissing" interactions. Nonetheless, their hybridization motives will lead to non-periodic aggregation to branched non-ordered nanostructures. Similarly, besides the self-assembly of the nucleic acid (**5**) to the tetragon-type structure, the inter-hybridization of complementary regions may lead to hairpin structures (such as Y, Z) that upon "kissing" interaction do not yield periodic ordered aggregated nanostructures. In fact, we were unable to design other foldable 2D topologies for the formation of the DNA nanotubes, except the respective hexagon- and tetragon- type arrangements.

The conformations and energetic of 4-way (Holiday) junctions have been studied extensively for over two decades.[34,36-40] It has been found that under low ionic salt conditions (corresponding to the conditions used in this study), even when single

junctions with 4-arm constructs are dispersed in solution, extended and close to square flat configurations dominate. [41] These structures tend to assume other less extended configurations when salt concentrations are higher. Similar findings have been reported for 3-way junctions. It is, therefore, reasonable to assume that within the context of an extended sheet with many repeating junctions, the overall configuration will be an extended, planar, configuration.

There have been less studies of the elastic properties of junctions with different topologies. Ascribing certain elastic properties to junctions could change out theoretical estimates to some extent. It is instructive to discuss 3 limiting cases: (i) that the bending rigidity of the junction κ_J is lower than κ_D, (ii) $\kappa_J \approx \kappa_D$, (iii) $\kappa_J > \kappa_D$. The last case (iii) has been extensively described in the previous sections. Interestingly, the result is not significantly altered also in case (ii). Because for this case the elastic constant is similar for DNA and junction, both will deform to the same extent (same strain) under any applied stress. However, the junction extends over a much smaller length when compared to the length of the polygon sides in the sheets. Therefore, this part will only account for a small percentage of the overall elastic energy (about 10% of the overall energy) as well as not modify the radius of the tube by much. In conclusion, for this case, the junction simply forms a small extension to the existing linear strand.

Finally, case (i) is the only one for which significant deviations from the predictions could be realized. Here, most of the strain is seen in the junction itself, and the stretches of dsDNA should remain almost unreformed. Similarly, the elastic energy stored in the junction will dominate over a negligibly small elastic energy stored in dsDNA. However,

because of the small linear extend of a junction, the bending rigidity of a junction should be at least 5-fold less than that of dsDNA for significant differences to be seen with respect to the other two scenarios discussed. Even assuming that $\kappa_J < \kappa_D$, it is unreasonable to expect the junction elasticity to be softer than the softest element in the system, namely that of single-stranded DNA. Studies show that for low salt content the persistence length of ssDNA is $\approx 7nm$, about 1/10 of that of ds DNA under similar salt conditions [42]. Supplementary Figure S9 shows calculations of the tetragonal sheets using this value for the junction bending rigidity compared with the case of junctions that are as stiff as dsDNA (case ii). The resulting predicted value for tube radius ($R^*_{\text{tetragons}} = 18nm$) is much smaller than those found experimentally or with the model prediction obtained with $\kappa_J \approx \kappa_D$ ($R^*_{\text{tetragons}} = 46nm$). Based on these calculations we conclude that junction bending rigidities that are much smaller than those of dsDNA are inconsistent with the experimental results. This has led us to use the assumptions previously discussed for all cases considered, yielding a self-consistent prediction for all that agrees well with the model parameters. Overall we find good validation for the model parameters in the experimental results.

Supplementary References

34. Seeman, N. C. DNA engineering and its application to nanotechnology. *Trends in Biotechnol.* **17**, 437-443 (1999).

35. Mosconi, F., Allemand, J. F., Bensimon, D. & Croquette, V. Measurement of the Torque on a Single Stretched and Twisted DNA Using Magnetic Tweezers. *Phys. Rev. Lett.* **102** (2009).

36. Person, B., Stein, I. H., Steinhauer, C., Vogelsang, J. & Tinnefeld, P. Correlated Movement and Bending of Nucleic Acid Structures Visualized by Multicolor Single-Molecule Spectroscopy. *ChemPhysChem* 10, 1455-1460 (2009).

37. Seeman, N. C. & Kallenbach, N. R. DNA Branched Junctions. *Annu. Rev. Biophys. Biomol.***23**, 53-86 (1994).

38. Srinivasan, A. R. & Olson, W. K. Computer Models of DNA Four-Way Junctions. *Biochemistry* **33** (1994).

39. Yang, M. & Millar, D. P. Conformational Flexibility of Three-Way DNA Junctions Containing Unpaired Nucleotides. *Biochemistry* **35** (1996).

40. Altona, C., Pikkemaat, J. A. & Overmars, F. J. J. Three-way and four-way junctions in DNA: a conformational viewpoint. *Curr. Opin. Struct. Biol.* **6**, 305-316 (1996).

41. Clegg, R. M., Murchie, A. I. & Lilley, D. M. The Solution Structure of the Four-Way DNA Junction at Low-Salt Conditions: A Fluorescence Resonance Energy Transfer Analysis. *Biophysical journal* **66**, 99-109 (1994).

42. Tinland, B., Pluen, A., Sturm, J. & Weill, G. Persistence Length of Single-Stranded DNA. *Macromolecules,* **30***,* 5763-5765 (1997).